Supporting Information

Huang et al. 10.1073/pnas.1603980113

SI Materials and Methods

Protein Expression and Purification. The *T. acidophilum* VAT gene (18) was cloned into a pProEx expression vector. The construct included an N-terminal His_6-tag and a tobacco etch virus (TEV) cleavage site engineered between the His_6-tag and the protein sequence. All mutants, including the cysteine-free VAT (C77A/C679A), VAT for cross-linking (K111C/K494C introduced into the cysteine-free construct), and VAT for $^{13}CH_3$-S labeling (K111C, M652C, and M684C introduced into cysteine-free VAT), were prepared with *PfuTurbo* DNA polymerase using the QuikChange site-directed mutagenesis method. Protein expression was achieved by growing transformed *Escherichia coli* BL21(DE3) cells in LB containing 100 mg/L ampicillin. Proteins were expressed at 37 °C for 4 h after induction with 1 mM isopropyl β-D-1-thiogalactopyranoside (IPTG) when the OD_{600} reached 0.8. For VAT variants used for NMR experiments (K111C, M652C, and M684C), transformed cells were grown in 99.9% D_2O and M9 medium with 3 g/L d7-glucose as the sole carbon source. Deuterated VAT variants were expressed at 25 °C overnight after induction with 1 mM IPTG at an OD_{600} of 0.8. For wt VAT, the cells were harvested and suspended in Ni-A buffer [50 mM Hepes, 200 mM NaCl, 10 mM imidazole (pH 7.5)], followed by lysis using sonication. After centrifuging the lysate at 39,200 × *g* for 30 min, the supernatant was filtered and applied to a HisTrap affinity column (GE Healthcare). The protein was washed with Ni-A buffer and eluted with Ni-B buffer [50 mM Hepes, 300 mM NaCl, 400 mM imidazole (pH 7.5)]. The His_6-tag was then cleaved by TEV (1:30 weight ratio of TEV to VAT) while dialyzing the protein solution overnight against buffer containing 25 mM Hepes, 50 mM NaCl, 1 mM EDTA, and 2 mM DTT (pH 7.5). After concentration, the protein was further purified on a HiLoad 16/60 Superdex 200 PG gel filtration column (GE Healthcare), equilibrated with 50 mM Hepes and 200 mM NaCl (pH 7.5). VAT variants eluted as a single peak at ∼62 mL, corresponding to a hexameric assembly of ∼500 kDa. The purity of the proteins was confirmed by SDS/PAGE and electrospray ionization-mass spectrometry. VAT mutants used for cross-linking or $^{13}CH_3$-S labeling were purified with the same protocol as described above, except that 5 mM DTT was added to the buffers and the final stock of the proteins. Before cross-linking/$^{13}CH_3$-S labeling, the proteins were buffer-exchanged into a DTT-free buffer [50 mM Hepes, 200 mM NaCl (pH 7.5)] using an Amicon Ultra-15 100K molecular weight cutoff filter (Millipore) until the final concentration of DTT was below 1 μM. To prepare VAT in the apo and ADP- and ATP/ATPγS-bound forms, purified VAT was first incubated with apyrase (New England Biolabs; 0.1 U of apyrase per milligram of VAT) at 25 °C overnight to obtain apo-VAT, followed by SEC to remove apyrase. Desired nucleotides were later added into apo-VAT at a final concentration of 5 mM to prepare VAT in different nucleotide states.

The half-proteasome ($\alpha_7\alpha_7$) labeled as [U-^{2}H; Ile$^{\delta1}$-$^{13}CH_3$; Leu,Val-$^{13}CH_3$,$^{13}CD_3$], used as a control in NMR diffusion measurements, and GroEL (D87K), used in the unfolding assay, were expressed and purified as described previously (30, 56).

Additional NMR Details. Translational diffusion constants for $^{13}CH_3$-S–labeled VAT samples were measured at 40 °C by recording a series of 2D ^{13}C-^{1}H correlation spectra as a function of the square of the labeling gradient (G^2), using a water-suppressed longitudinal encode decode (SLED)-based pulse scheme that is similar to a previously published ^{15}N-edited experiment (47). A related approach was used for the measurement of diffusion of the half-proteasome $\alpha_7\alpha_7$, except that a series of 1D ^{13}C-edited ^{1}H spectra were obtained (40 °C) and the ^{1}H signal was integrated within a frequency range extending from 1–3 ppm to obtain the intensity at each gradient strength. A constant-time diffusion period of 200 ms was used for all measurements. Diffusion constants were obtained by nonlinear least-squares fitting of peak intensities as a function of the square of the gradient-encoding pulses using the relation $I = I_0\exp(-ADG^2)$, I and I_0 are peak intensities in the presence and absence of gradient G, respectively, D is the diffusion constant and A is a constant that depends on the experimental parameters.

A 2D ^{13}C-^{1}H heteronuclear single quantum coherence (HSQC)-based magnetization exchange experiment was recorded, as described previously (75), at 60 °C using a mixing time of 0.9 s (Fig. S8). A sample of VAT-ADP was chosen for a number of reasons. First, ATPγS is hydrolyzed over time by VAT, precluding studies of VAT-ATPγS over the lengthy time course that is required to perform these experiments (typically 1–2 d). Second, state A is more populated for VAT-ADP than VAT-ATPγS (28% vs. 8%), increasing the sensitivity of the ADP-based experiments. It is worth recalling that states A and B do not refer to the stacked- and split-ring VAT conformers, but rather derive from protomers 5–6 and 1–4, respectively, of the split-ring (as discussed in the main text). In the case of a sample with VAT exclusively in the stacked-ring conformation, only B state peaks would be observed.

The $R_{2,S}$ rates for the slowly relaxing ^{1}H methyl component of magnetization were measured at 60 °C using a pulse scheme previously described (49). The relaxation delays used were 0.002, 0.005, 0.008, 0.011, 0.015, and 0.020 s with relaxation rates obtained by fitting peak intensities to single exponential decay functions, $y = A\exp(-R_{2,S}T)$. Experiments were repeated with stepwise additions of 0.5 mM Gd(III)DTPA-BMA into the protein solution. All spectra were processed using the NMRPipe program (76) and visualized and analyzed using NMRPipe and Sparky (77).

Cryo-EM Image Processing. Whole-frame alignment was performed with *alignframes_lmbfgs* (78), and the resulting averages of frames were used for contrast transfer function (CTF) determination with CTFFIND4 (79) and automated particle selection with RELION (55, 80). Particle coordinates were used to extract the particle images in 256 × 256-pixel boxes from the unaligned movies while performing individual particle alignment and exposure weighting with *alignparts_lmbfgs* (78). Magnification was corrected for a previously described 2% anisotropy (81), resulting in a calibrated pixel size of 1.45 Å. For the ADP-loaded state, a total of 154,699 candidate particle images were subjected to 2D and 3D classification without symmetry in RELION, yielding a single 3D class containing 71,258 particle images, which were then subjected to refinement and sharpening in RELION (55). Initial rounds of 3D classification used a low-pass-filtered map of p97 as a reference (82). Subsequent rounds of 3D classification used low-pass-filtered versions of the split-ring conformation. For the ATPγS-loaded state, a total of 39,803 candidate particle images were subjected to 2D classification. The 31,839 particle images giving 2D classes that showed views of the complex were subjected to 3D classification with five classes, from which two interpretable maps were obtained: the split-ring conformer and the stacked-ring conformer.

Map Analysis and Model Building. Homologs of *T. acidophilum* VAT were identified in the National Center for Biotechnology Information (NCBI) nonredundant protein sequence database with PSI-BLAST (83) (E-value threshold of 0.005). The collected sequences were clustered at 90% sequence identity with CD-HIT (84), and multiple sequence alignment was generated with PCMA (85). Protein secondary structure was predicted with PSIPRED (86). The crystal structure of *M. musculus* p97 (PDB ID code 3CF3) was selected as a template for homology modeling after analyzing the results of the GeneSilico Metaserver (87). The NTDs were based on the NMR structure for VAT (PDB ID code 1CZ4). The sequence-to-structure alignment between VAT and the template was built using the consensus alignment approach and 3D assessment (88) based on the results of FFAS (89), HHsearch (90), and BLASTp. In addition, the multiple sequence alignment of the family, secondary structure predictions, the conservation of critical active site residues, and hydrophobic patterns were taken into account. The 3D model of VAT was built with MODELER (91). Model quality assessment was carried out with ProSA-web server (92).

Segmentation of maps was performed with UCSF Chimera (93, 94). Each monomer was segmented, and the homology model was fit into the density using NAMD with molecular dynamics flexible fitting with a density scaling factor of 0.1 over 100,000 steps (100 ps) (43). To limit effects of fitting side chains, for which density is not present in the map, only backbone atoms were included in the molecular dynamics simulation. All images of maps and models, as well as the movie of molecular motion (Movie S1), were rendered using USCF Chimera.

EM Population Analysis. To determine the relative populations of the split-ring and stacked-ring classes in the ATPγS dataset, particle images selected after 2D classification in RELION were randomly split into three groups for 3D classification. Each group was subjected to 3D classification using both a split-ring and stacked-ring starting reference, low-pass-filtered to 40 Å. The ratio of particle images in split-ring classes to stacked-ring classes was calculated for each starting model. A paired Student's *t* test comparing runs using different starting models had a *P* value of 0.22, showing that no significant bias was introduced by the starting model.

Cross-Linking of VAT. After removing DTT from the storage buffer, VAT mutants (K111C/K494C) were diluted to a final protein concentration of 5 μM to reduce intermolecular cross-linking, and 5 mM ADP was subsequently added. Disulfide oxidation was catalyzed by addition of 20 μM copper-1,10-phenantroline, followed by incubation at 37 °C for 0.5 h. The reaction was then quenched by the addition of 5 mM EDTA, and 1 mM maleimide was added to react with the remaining free cysteines to prevent further formation of dodecamer and higher oligomers. The products were separated with a gel filtration column (Superdex 200 16/60; GE Healthcare) and then analyzed by native and SDS/PAGE electrophoresis under nonreducing conditions.

$^{13}CH_3$-S Labeling with MMTS. ^{13}C-MMTS was stored at a concentration of 100 mM in DMSO at −20 °C. Labeling was achieved using an approach described previously (46). Briefly, following buffer exchange of the purified VAT mutants (K111C, M652C, and M684C) into a DTT-free buffer, ^{13}C-MMTS stock solution was added at 50% molar excess (over protein) and the reaction at room temperature was left overnight. Unreacted ^{13}C-MMTS was removed by buffer exchange of the product into NMR buffer [25 mM potassium phosphate, 50 mM NaCl, 4.3 mM NaN_3, 1 mM EDTA (pH 7.5) in 99.9% D_2O].

Functional Assays. ATPase activities of wt and cross-linked VAT (111C-494C; VAT*) were measured using a NADH-coupled assay that has been described previously (95, 96). The reaction was carried out using a VAT concentration of 0.83 μM (in hexamer) and included an ATP-regeneration system that contained 2.5 mM phosphoenolpyruvate, 0.2 mM NADH, 50 μg/mL pyruvate kinase, 50 μg/mL lactate dehydrogenase, and 3 mM ATP. The reaction was monitored in a UV-visible spectrometer by the change in the absorbance at 340 nm at 25 °C. All measurements were performed in triplicate.

Unfolding activities of wt VAT and VAT* were measured by monitoring the loss of fluorescence of a green fluorescent protein substrate with an 11-residue ssrA extension at its carboxyl terminus, GFP11, following the protocol of Horwich and coworkers (56). A hexameric concentration of 8.5 μM VAT was mixed with 1 μM GPF11 and 1.6 μM GroEL (D87K); the latter serves as a "trap," capturing unfolded GFP11 and keeping it in a nonnative state. The reactions were carried out in the presence and absence of 2 mM DTT, with and without 50 mM ATP, and the total reaction volume was 100 μL [50 mM Hepes, 200 mM NaCl, 120 mM $MgCl_2$ (pH 7.5)]. Fluorescence of GFP11 was monitored as a function of time in a fluorescence plate reader with fluorescence excitation at 480 nm and emission at 520 nm. Initial slopes were recorded to calculate the initial unfolding rate of GFP11.

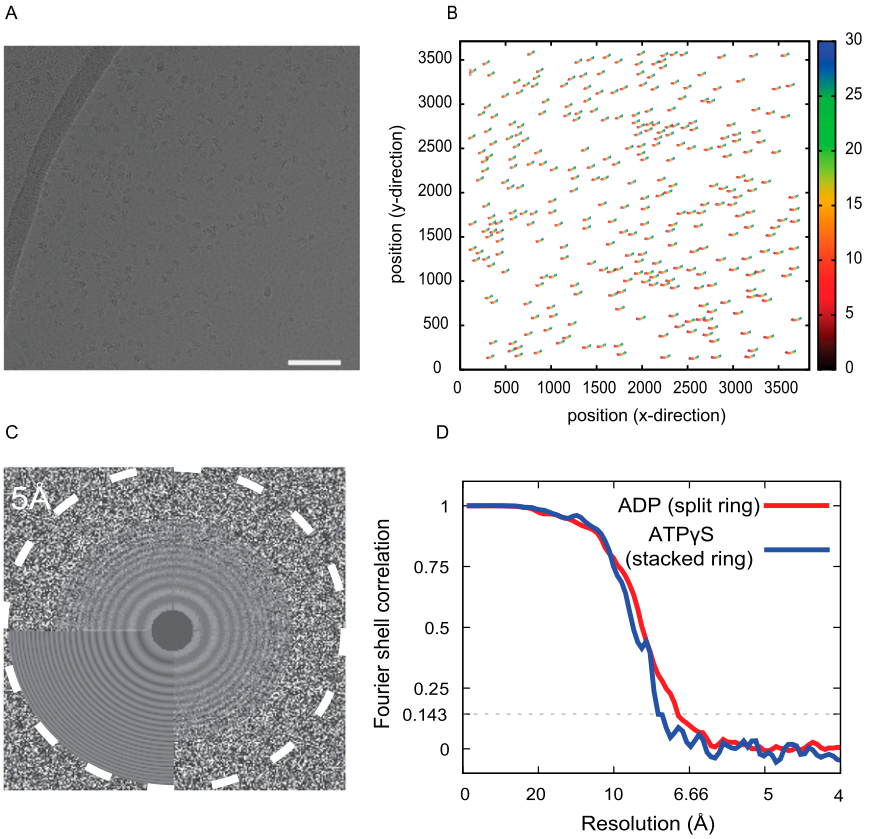

Fig. S1. (*A*) Sample micrograph region from the ADP-loaded VAT dataset. (Scale bar, 500 Å.) (*B*) Example of particle trajectory measurement used for drift correction, from *alignparts_lmbfgs* (78) (trajectories exaggerated fivefold). (*C*) Sample micrograph power spectrum, with the modeled power spectrum from CTFFIND4 (79) in the lower left quadrant. (*D*) Fourier shell correlation curves are shown for the ADP- and ATPγS-loaded states, and report the same resolution as a curve obtained with phase randomization to correct for masking effects.

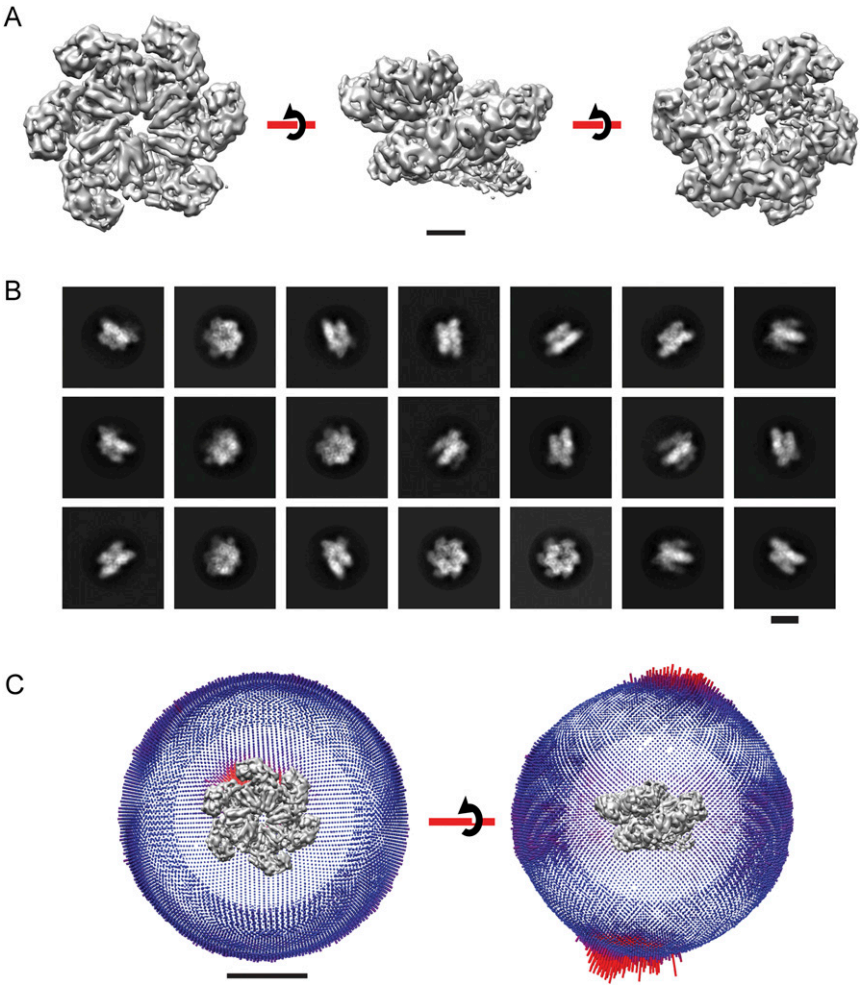

Fig. S2. (*A*) Top, side, and bottom views of the ADP-loaded VAT complex at 7.0-Å resolution. (Scale bar, 25 Å.) (*B*) Representative 2D class averages for the ADP-loaded VAT complex selected for 3D classification and refinement. (Scale bar, 100 Å.) (*C*) Distribution of calculated Euler angles is represented as a sphere surrounding the map, where the height of the different rods and transition from blue to red denote the relative number of particle images that were aligned at that orientation. (Scale bar, 100 Å.)

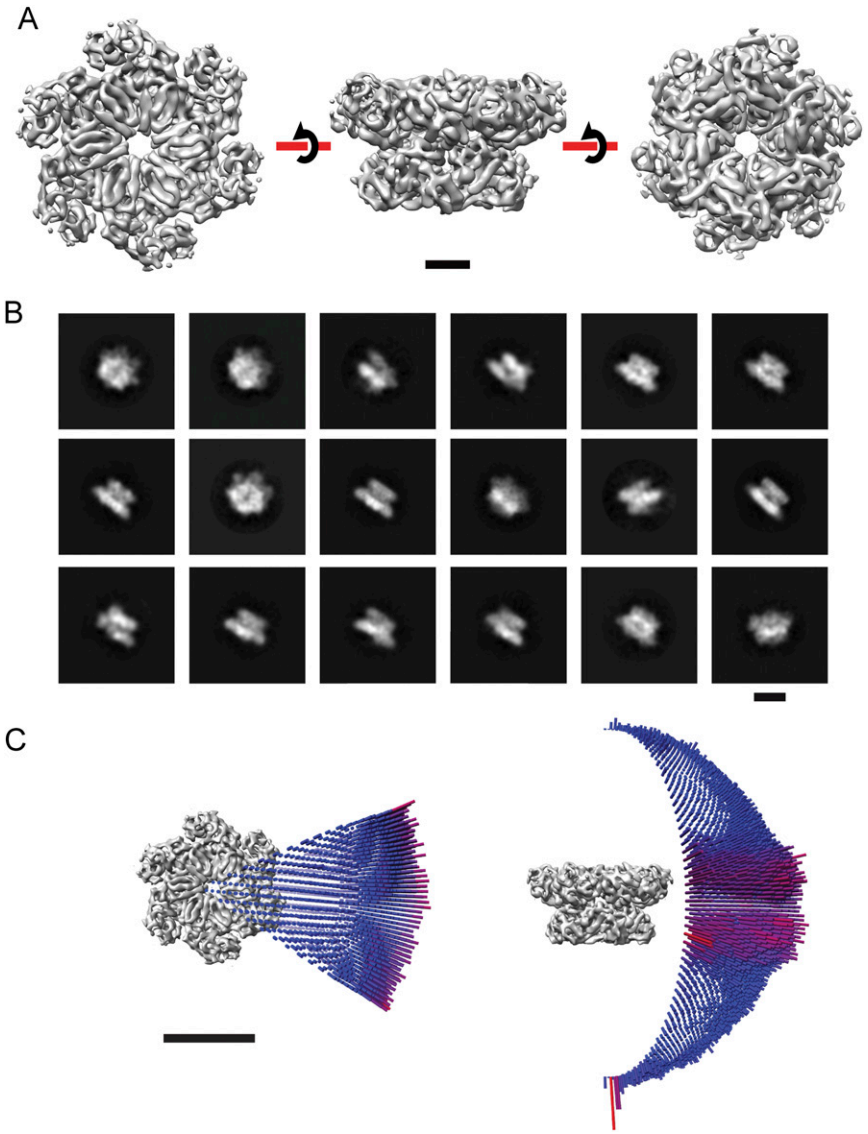

Fig. S3. (*A*) Top, side, and bottom views of the ATPγS-loaded VAT complex in the stacked-ring conformation at 7.8-Å resolution. (Scale bar, 25 Å.) (*B*) Representative 2D class averages for the ATPγS-loaded VAT complex selected for 3D classification and refinement. (Scale bar, 100 Å.) (*C*) Distribution of calculated Euler angles is represented as a sphere surrounding the map, where the height of the different rods and transition from blue to red denote the relative number of particle images that were aligned at that orientation. (Scale bar, 100 Å.)

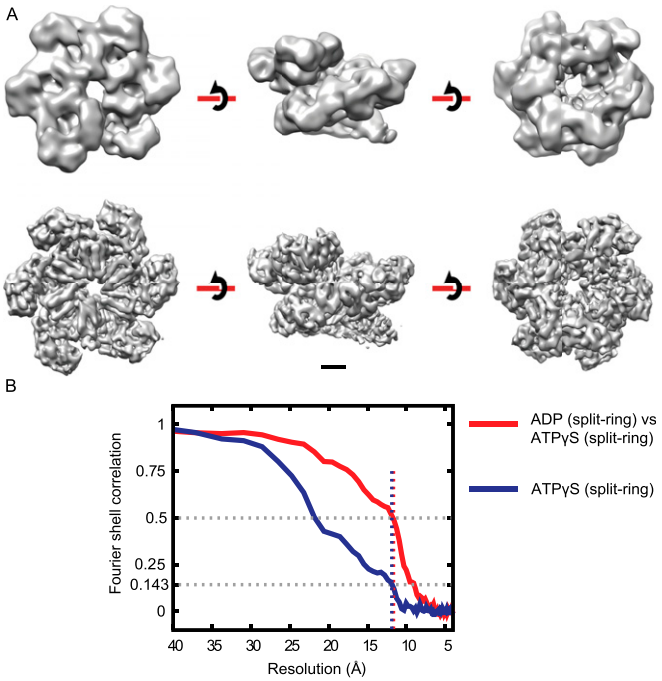

Fig. S4. (*A*) Top, side, and bottom views of the split-ring conformation from both the ATPγS-loaded (*Upper*) and ADP-loaded (*Lower*) states. (Scale bar, 25 Å.) (*B*) Fourier shell correlation (FSC) curve for the ATPγS-loaded split ring (12 Å at FSC = 0.143) is shown in blue. The FSC curve between aligned maps of the ADP-loaded split-ring and the ATPγS-loaded split-ring is colored in red and shows FSC = 0.5 at 12 Å, indicating that these conformations are statistically identical up to this resolution. The FSC curves report the same resolutions as curves obtained with phase randomization to correct for masking effects.

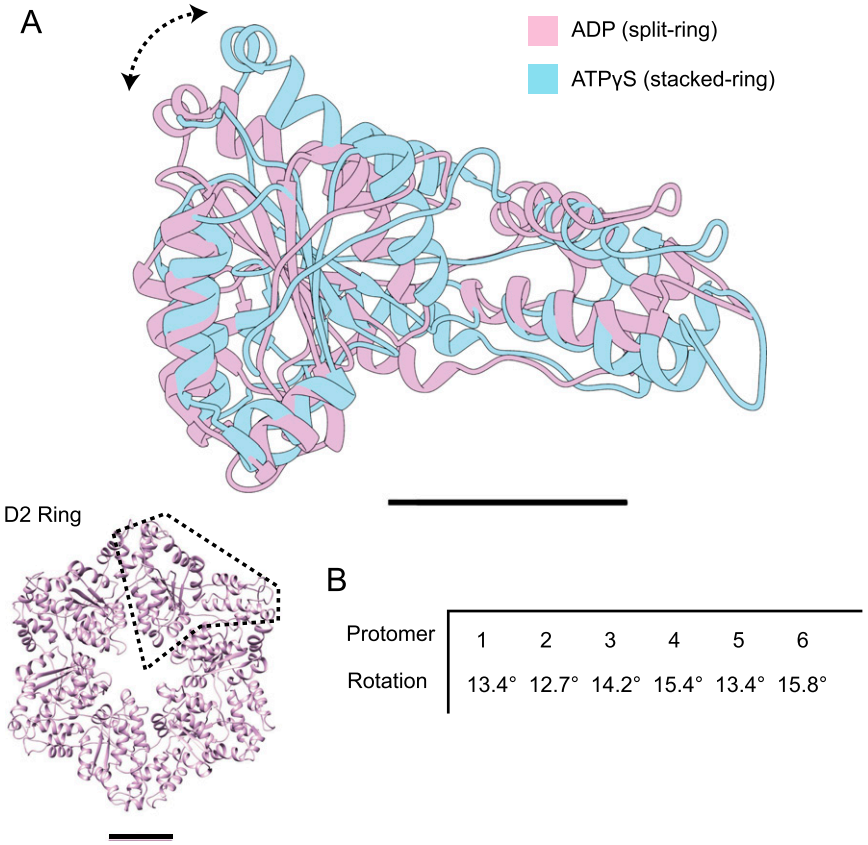

Fig. S5. (*A*) Superposition of D2 domains from ADP-loaded (split-ring) and ATPγS-loaded (stacked-ring) states after alignment of the D1 domains shows that the splitting of the ring is accompanied by a rotation of the D2 domain relative to the D1 domain in each protomer. (*Inset*) D2 ring of the ATPγS-loaded stacked-ring conformation. One of the six protomers is enclosed by dashed lines. (Scale bars, 25 Å.) (*B*) Measured rotation of the D2 domains of ADP-bound protomers 1–6 relative to the D2 domain of the ATPγS-loaded stacked-ring conformation. Rotations were calculated with UCSF Chimera (93).

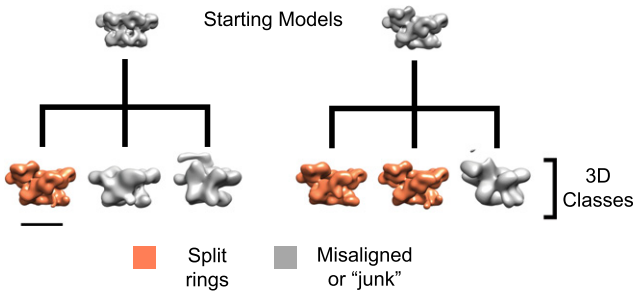

Fig. S6. Cross-linked VAT was incubated with ATP, frozen, and imaged as described in *Materials and Methods*. Maps produced from 3D classification reveal that only the split-ring conformation is seen for cross-linked VAT, regardless of the starting model used for 3D classification. (Scale bar, 100 Å.)

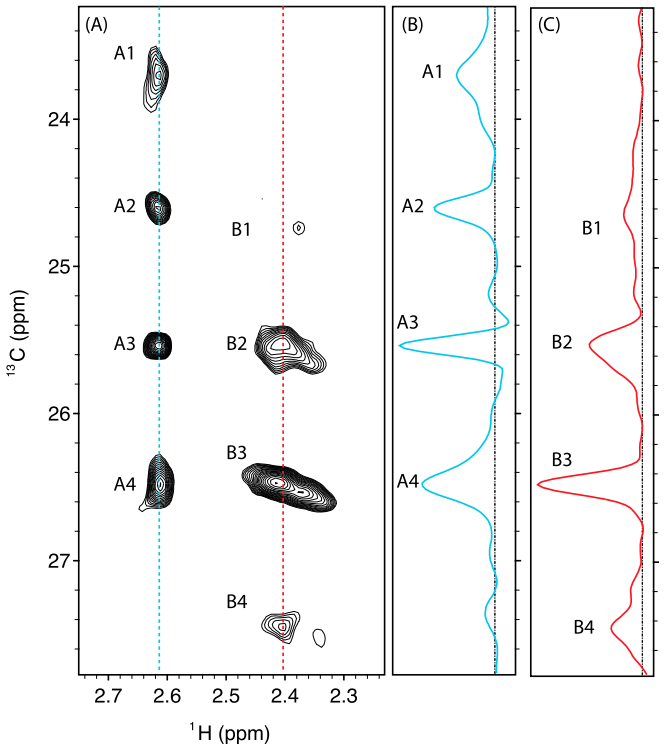

Fig. S7. F_1-coupled ^{1}H-^{13}C HSQC spectrum confirms higher mobility of the 684 $^{13}CH_3$-S probe in protomer 6 of ADP-VAT. (*A*) ^{1}H-coupled ^{1}H-^{13}C HSQC spectra (recorded at 600-MHz ^{1}H frequency, 60 °C) of M684C-$^{13}CH_3$ ADP-VAT showing the quartet structure of peaks A and B that results from the one-bond ^{1}H-^{13}C scalar coupling (125 Hz). (*B* and *C*) Vertical slices taken at ^{1}H chemical shifts corresponding to peaks A (cyan) and B (red) show that the intensities are significantly different from 3:1:1:3, which is expected in the absence of relaxation. The effects of relaxation are more significant for peak B, consistent with decreased mobility in this state relative to peak A. Note that the multiplet components are not symmetrical due to relaxation interference effects between ^{1}H-^{13}C dipolar and ^{13}C chemical shift anisotropy interactions.

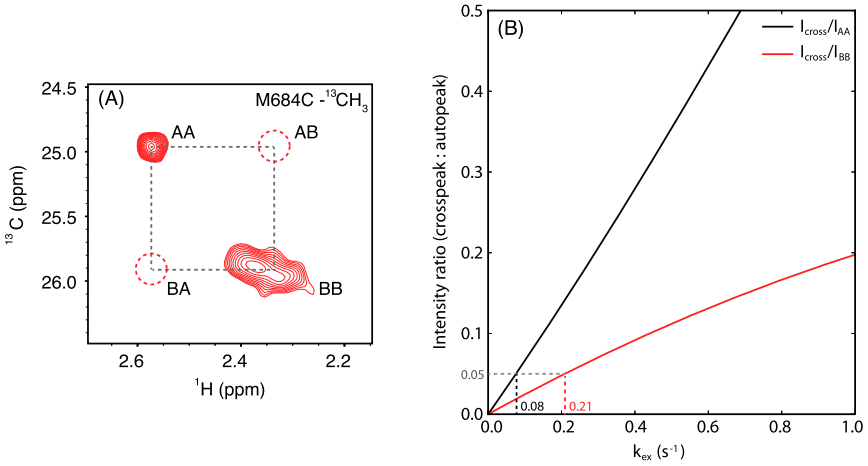

Fig. S8. Magnetization exchange spectroscopy (47) establishes that the rates of interconversion between states A and B in ADP-loaded VAT are less than ~0.2 s^{-1}. (*A*) Magnetization exchange spectrum (600 MHz, 60 °C) recorded with a mixing time of 0.9 s shows no exchange cross-peaks at position AB or BA. Note that the intensities of the AB and BA cross-peaks are expected to be the same, assuming similar relaxation times in each state and similar processing in each of the t_1 and t_2 dimensions. (*B*) Simulation of intensity ratios of cross-peaks and diagonal peaks as a function of the exchange rate, $k_{ex} = k_{AB} + k_{BA}$, assuming a two-site exchange model (97), where nuclei in both states A and B have identical longitudinal relaxation rates (1 s^{-1}, verified experimentally), using a mixing time of 0.9 s and fractional populations of states A and B of 27.8% and 72.2%, respectively (based on areas of peaks in HMQC spectra).

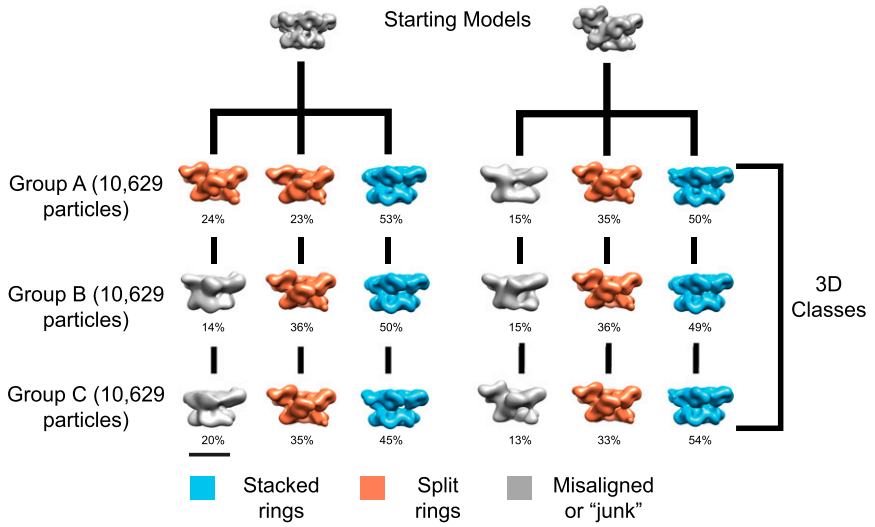

Fig. S9. Initial references and resulting maps from 3D classification of the ATPγS-loaded VAT dataset. Classification was done in triplicate by dividing the dataset into three independent nonoverlapping groups of particle images, and subsequently subjecting particle images in those groups to 3D classification. Relative populations of each class are labeled beneath each map. (Scale bar, 100 Å.)

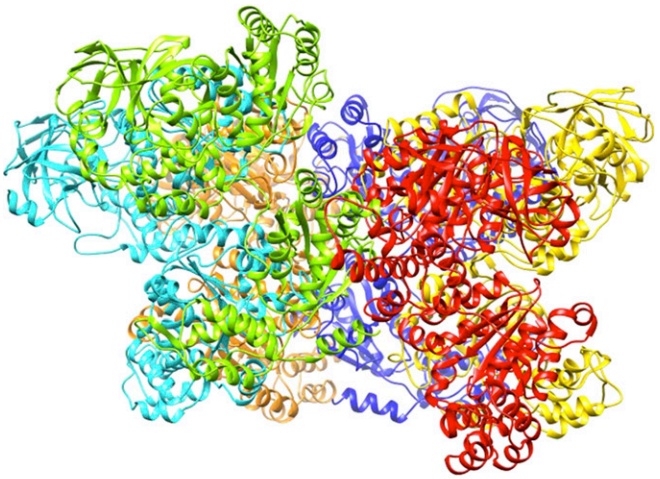

Movie S1. Interpolation between the split- and stacked-ring structures of the VAT complex. Experimental map densities are shown for the two end points of the interpolation. (Scale bar, 25 Å.)

Movie S1